# Nonlinear Quantum Photonics with a Tin-Vacancy Center Coupled to a One-Dimensional Diamond Waveguide

Matteo Pasini, Nina Codreanu, Tim Turan, Adrià Riera Moral,* Christian F. Primavera, Lorenzo De Santis, Hans K. C. Beukers, Julia M. Brevoord, Christopher Waas, Johannes Borregaard,† and Ronald Hanson‡
*QuTech and Kavli Institute of Nanoscience, Delft University of Technology, P.O. Box 5046, 2600 GA Delft, The Netherlands*

(Received 22 November 2023; accepted 13 May 2024; published 9 July 2024)

Color centers integrated with nanophotonic devices have emerged as a compelling platform for quantum science and technology. Here, we integrate tin-vacancy centers in a diamond waveguide and investigate the interaction with light at the single-photon level in both reflection and transmission. We observe single-emitter-induced extinction of the transmitted light up to 25% and measure the nonlinear effect on the photon statistics. Furthermore, we demonstrate fully tunable interference between the reflected single-photon field and laser light backscattered at the fiber end and show the corresponding controlled change between bunched and antibunched photon statistics in the reflected field.

DOI: 10.1103/PhysRevLett.133.023603

Nonlinear interactions between single photons and solid-state color centers are at the heart of many applications in quantum science [1,2] such as the realization of a quantum internet [3,4]. In particular, color centers in diamond have enabled advanced demonstrations in this direction showing multinode quantum network operation [5,6], memory-enhanced communication [7], and scalable on-chip hybrid integration [8]. Among the diamond color centers, the tin-vacancy center (SnV) has recently emerged as a promising qubit platform, as it combines the inversion symmetry of group-IV color centers [9,10], allowing for integration in nanophotonic structures, with good optical properties [11–14] and above-millisecond spin coherence at temperatures above 1 K [15,16]. Devices combining photonic integration with spin and optical control could serve as a future scalable building block for realizing spin-photon gates [17]. On the path toward such scalable on-chip integration, incorporation of emitters into nanophotonic waveguides [12,18] enables exploration of the coherent emitter-photon interaction typical of waveguide-coupled systems [19,20]. Compared to nanophotonic cavities [21], waveguides have the advantages of being broadband, eliminating the challenge of cavity tuning, and of having significantly higher error tolerance in fabrication.

In this Letter, we present a device consisting of a SnV center coupled to a nanophotonic diamond waveguide with tapered-fiber access, depicted in Fig. 1(a). Thanks to efficient coupling, double-sided access, and real-time charge-resonance checks, we are able to perform a comprehensive investigation of the nonlinear interaction of the color center with the waveguide mode in both transmission and reflection. We observe the extinction of transmitted light which arises from interference between the photons interacting with the emitter and the single optical mode of the waveguide [22,23], from which we quantify the coupling strength of the SnV to the waveguide. In the reflected signal, we observe interference between single photons scattered by the emitter and a classical reflection of the probe laser. The tunability of our device enables us to map out the various regimes of interference and their corresponding photon statistics.

Our device is fabricated in two main phases. First, SnV centers are generated by implantation on an electronic-grade diamond of $^{120}$Sn ions at a target depth of ∼88 nm, followed by an annealing step to create SnV centers. On the sample, we then fabricate suspended waveguides that support a single TE mode for SnV emission. The fabrication is based on the crystal-dependent quasi-isotropic-etch undercut method [8,13,24–27]. We first pattern a hard mask material $Si_3N_4$, followed by the transfer pattern into the diamond substrate and vertical coverage with $Al_2O_3$ of the structures sidewalls. Next, the quasi-isotropic etch undercuts the devices, followed by an upward etch to thin the devices down to a thickness of ≈250 nm. The fabrication concludes with an inorganic removal of the hard mask materials. The details of the fabrication can be found in Supplemental Material [28].

Our fabrication differs from earlier work [8,13,24–26] in one main aspect: We demonstrate successful quasi-isotropic undercut of the waveguides at a considerably lower temperature of the reactor wafer table of only 65 °C. We show that the quasi-isotropic crystal-dependent reactive-ion

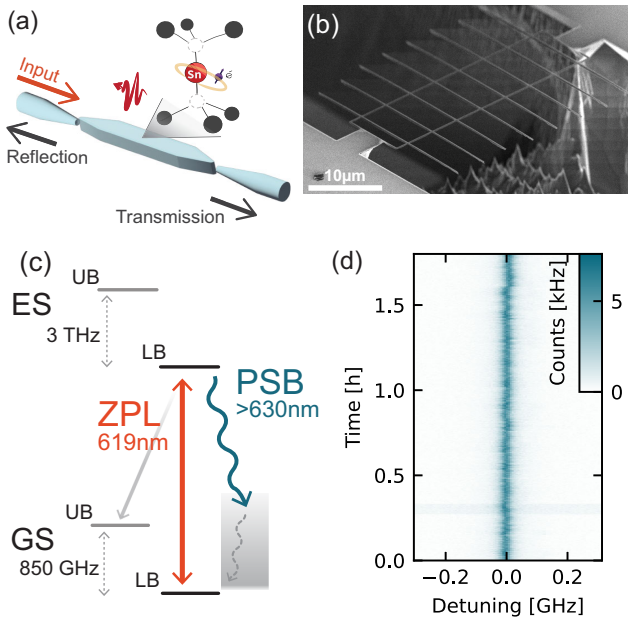


FIG. 1. Device and optical transition properties. (a) Schematic of the device and the fiber coupling. (b) SEM image of one entire diamond device chip. (c) Energy level scheme of the SnV. At 5 K, the SnV spectrum shows two ZPL transitions between the lower branch (LB) of the excited state (ES) to the lower (upper) branches (LB) [(UB)] of the ground state (GS). Here, we focus on the ZPL transition between LB of ES and LB of GS at 619 nm, and we filter the other ZPL out. Phonon-assisted decay from the excited state gives rise to a phonon sideband (PSB) with a broad optical spectrum above 630 nm. (d) Consecutive photoluminescence excitation (PLE) scans conditioned on the SnV being in the right charge and frequency state. The scanning speed of each PLE is ∼300 MHz/s.

etch in this temperature regime is successfully undercutting the waveguide structures without the need of an optional $O_2$ anisotropic etch step following the vertical sidewalls coverage with $Al_2O_3$. This has the key benefit of preserving the hard mask aspect ratio, without further edge mask rounding stemming from the $O_2$ etch.

The fabricated devices consist of arrays of double-sided tapered waveguides, anchored to the surrounding bulk substrate by a square support structure, as seen in Fig. 1(b). To couple light in and out of the waveguide, we use optical fibers that are etched into conical tapers in hydrofluoric acid [37]. We position the fibers in front of the waveguide and exploit the lensing effect of the taper, as illustrated in Fig. 1(a). We choose this method as it allows easy variation of the distance between fiber and waveguide. This will later be used to tune the phase of the reflected signal. All experiments are performed at 5 K in a closed-cycle cryostat, with no external magnetic field. Within the SnV level structure [Fig. 1(c)], we focus on the optical zero-phonon line (ZPL) transition between the lower branches of the ground and excited states, of wavelength around 619 nm. Spontaneous emission from the excited state can also happen with a phonon-assisted process, giving rise to a phonon sideband (PSB).

We investigate the optical stability of one emitter [red arrow in Fig. 1(d)] by performing consecutive photoluminescence excitation (PLE) scans. The scans are preconditioned on a successful charge-resonance check [14]: Before each scan, we turn on the probe laser at a set frequency and count how many PSB photons are detected. A threshold number of counts is chosen to make sure that the SnV is in the desired charge state and on resonance with the emitter (see Supplemental Material [28]). This heralding technique mitigates the effects of emitter ionization and of spectral diffusion [14].

Summing data from 1.8 h of continuous measurement [Fig. 1(e)], we observe an integrated linewidth of $(38.0 \pm 0.3)$ MHz, very close to the average linewidth of the single scans of $(32.1 \pm 0.1)$ MHz, indicating that there is very little effective spectral diffusion in our measurements. This can, in principle, be further improved by increasing the conditioning threshold at the expense of experiment speed. All the measurements reported below are conditioned on a charge-resonant check with similar threshold. By measuring second-order photon correlations using different resonant laser powers (see Supplemental Material [28]), we extract the excited state lifetime of the emitter to be $(5.91 \pm 0.08)$ ns, corresponding to a transform-limited transition linewidth of $(26.7 \pm 0.3)$ MHz. This value is close to the average single scan linewidth, indicating that there is little residual broadening of the transition.

To probe the coupling of the SnV center to the waveguide, we scan the probe laser across the transition frequency while simultaneously collecting both the transmitted and reflected signals. We spectrally filter the signals and record both ZPL and PSB (separately) in the reflected output port and the ZPL in the transmission output port (see Supplemental Material for details). This simultaneous measurement allows us to monitor the SnV behavior through the PSB emission while observing its coherent interaction with the input probe through the ZPL signal [Fig. 2(a)].

We observe a significant extinction of the transmission signal on resonance, indicating a coherent light-matter interaction in our waveguide-QED system [23]: Destructive interference between scattered photons and the transmitted field causes the emitter-induced reflection of single photons. The magnitude of the transmission dip contrast on resonance is determined by the emitter-waveguide coupling factor $\beta = \gamma_{wg}/\gamma_{tot}$, where $\gamma_{wg}$ $(\gamma_{tot})$ is the decay rate into the waveguide (the total decay rate of the excited state). In particular, in the absence of dephasing of the optical transition, the transmission behavior is described by [19]

$$T(\omega) = \left| 1 - \frac{\beta}{\left(1 + \frac{\langle n \rangle}{n_c}\right)\left(1 + \frac{2i\omega}{\gamma_{tot}}\right)} \right|^2, \qquad (1)$$

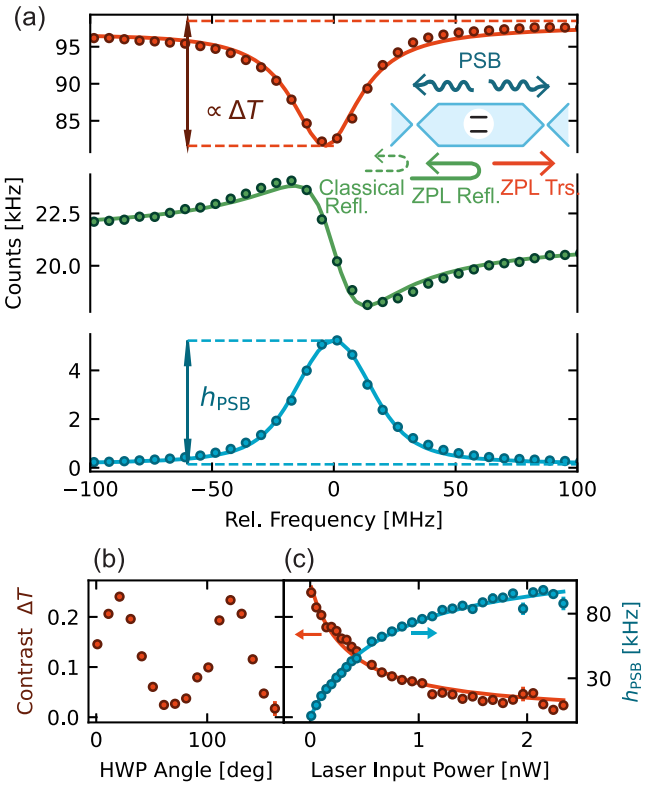


FIG. 2. Spectroscopy of the waveguide-SnV system. (a) Simultaneous measurement of transmitted ZPL light through the system (top), reflected ZPL light (center), and PSB emission (bottom) while scanning the probe laser. The inset shows a schematic of the system; the colors represent the different channels measured. We highlight the transmission contrast $\Delta T$ and the peak height of the PSB emission scan $h_{\mathrm{PSB}}$. (b) Contrast of the transmission extinction when varying the input fiber polarization using a half wave plate (HWP). (c) Transmission contrast and PSB peak height as a function of the power in the input fiber showing saturation of the SnV response when the average photon number increases. In the low-power range, we observe a maximum transmission extinction of $0.25 \pm 0.01$.

where $\omega$ is the detuning of the probe laser from the emitter, $\langle n \rangle$ is the average photon number per lifetime in the input state, and $n_c = (1/4\beta^2)$ is the critical photon number, which indicates saturation of the photon-emitter interaction. In the limit of low excitation ($\langle n \rangle \ll n_c$), the transmission contrast on resonance $\Delta T = 1 - T(\omega = 0)$ is, thus, related to the coupling factor $\beta$ as $\Delta T = \beta(2 - \beta)$. Note that, in this analysis, we ignore the small additional broadening of the optical transition due to dephasing, making our estimates for $\beta$ a strict lower bound.

Experimentally, the value of the coupling factor $\beta$ can be reliably extracted by measuring the transmission contrast as a function of input laser power, given that $\langle n \rangle / n_c = P/P_c$ with $P_c$ the input power that saturates the interaction. To ensure that we are optimally coupling the probe field with the linear dipole of the optical transition, we sweep the polarization of the input field to find the maximal transmission contrast [Fig. 2(b)]. Fitting Eq. (1) to the measured transmission contrast as a function of input power [Fig. 2(c)], we obtain $\beta = 0.143 \pm 0.005$. This value is in good agreement with numerical simulations for our waveguide geometry (see Supplemental Material [28]) taking into account the emitter depth resulting from the implantation, a small lateral offset (≈50 nm) from the waveguide center, and the total efficiency of the transition of interest of 0.37 [38], obtained by combining quantum efficiency (0.8) [39], Debye-Waller factor (0.57) [40], and branching ratio between the two ZPL transitions (0.8) [13].

The critical laser power at the fiber input, $P_c$, corresponds to the critical photon number $n_c$ at the SnV center: $P_c = \eta^{-1} h\nu n_c \gamma$, where $\eta$ is the fiber-waveguide coupling efficiency, $\nu$ is the probe laser frequency, and $\gamma$ is the decay rate related to the excited state lifetime. From the fit value $P_c = (0.32 \pm 0.02)$ nW and knowing $n_c \sim 12$ photons from the value of $\beta$, we determine the fiber-waveguide coupling efficiency to be $\eta = 0.33 \pm 0.02$.

The reflection signal contains the single photons coherently reflected by the SnV center, interfering with classical reflection of the probe laser at the tapered fiber end. In a simplified picture, considering a Lorentzian response of the SnV, the reflection signal can be modeled as [18,41]

$$R(\omega) = \left| 1 + \xi \frac{1}{1 - 2i\omega/\gamma_{\mathrm{tot}}} e^{i\phi} \right|^2, \tag{2}$$

where $\xi$ is the ratio between the reflected single photons and the coherent state amplitude, which gives the average number of photons per lifetime in the input field, and $\phi$ is the phase difference between the coherent and single-photon components.

The emitter-induced single-photon nonlinear reflection alters the photon statistics of the transmitted and reflected fields, as we expose below by measuring the second-order correlation for different combination of signals.

We start by correlating the transmitted signal with itself. The emitter can reflect only one photon per its optical lifetime. When two indistinguishable photons coherently scatter on the emitter within the timescale of its optical lifetime, the nonlinear interaction results in a strongly correlated two-photon bound state that is perfectly transmitted [42]. In the case of $\beta \to 1$, the wave function of the scattered light is dominated by this bound-state component, resulting in strong bunching of the transmitted light [22]. In our case, however, the bound-state contribution is suppressed compared to the uncorrelated scattering of the two photons involving other channels. In other words, the probability that one of the two photons is incoherently scattered is higher than the probability of emitting the two-photon bound state in the waveguide. In this regime, upon detection of a photon in the transmission signal, the conditional probability of a second ZPL photon detection within the lifetime is suppressed compared to the steady

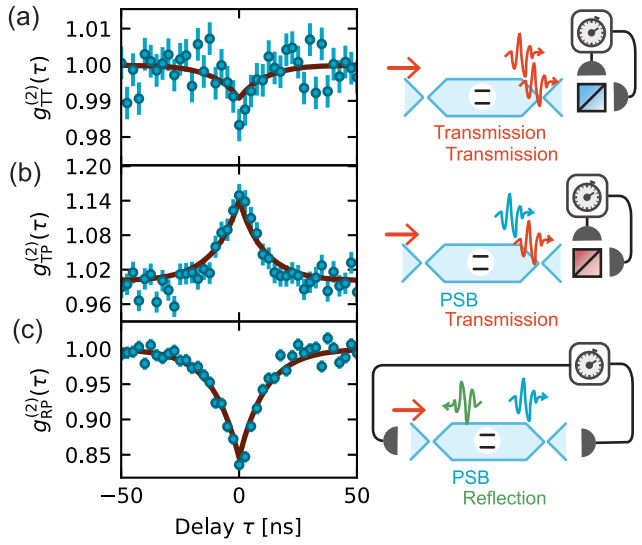


FIG. 3. Second-order correlation between (a) two transmitted photons, (b) a PSB and a transmitted photon, and (c) a PSB and a reflected photon in the constructive interference regime (see the main text and Fig. 4 for details). The blue dots are experimental data, and the red line is the theoretical model, where the relevant parameters are extracted by fitting corresponding reflection and transmission spectra.

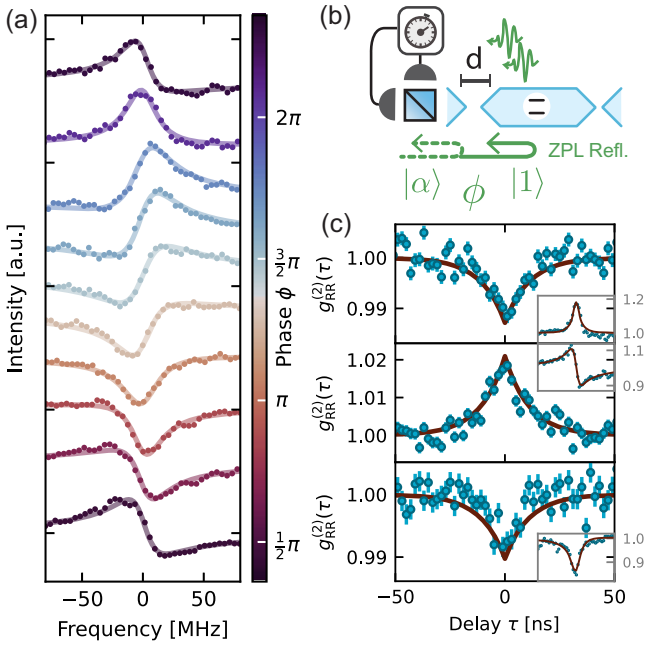


FIG. 4. Reflection measurements. (a) Reflection spectra at different fiber distance $d$, corresponding to different relative phase between the single photon and coherent state components. The solid line is a fit with the simplified model of Eq. (2); from this, we extract the phase $\phi$ which is indicated by the color bar. (b) Schematic of the measurement setting. (c) Second-order correlation of reflected photons in the constructive (top), dispersive (center), and destructive (bottom) interference regimes. The inset shows the reflection spectrum. We fit the reflection spectrum using Eq. (2) to extract $\phi$ and $\xi$, which we use as an input to the theoretical model. The red lines, in both the inset and the main figure, are the results of the theoretical model with the supplied parameters. The $x$ axis in the inset is frequency, ranging from −80 to 80 MHz.

state value. In full agreement with the predictions in Ref. [22], we find that this results in antibunching in the photon statistics for the transmission $g^{(2)}_{\mathrm{TT}}$ [Fig. 3(a)].

Since we have access to one of the incoherent decay channels, namely, the photons emitted in the PSB, we can verify that the effect on the photon statistics is induced by the coherent interaction of light with the emitter. We measure the probability of detecting a transmitted [Fig. 3(b)] or reflected photon [Fig. 3(c)] conditioned on the emission of a PSB photon. Detecting a PSB photon heralds an incoherent interaction which results in a higher probability of detecting a ZPL photon in the transmission port and a lower probability of detecting a ZPL photon in the reflected port, leading to the observed bunching and antibunching, respectively.

We compare the results in Fig. 3 with numerical simulations (the red lines in the figures), where the system is modeled as a lossy cavity coupled to an emitter (see Supplemental Material for details [28]). Using values for the model parameters extracted from fits to the corresponding transmission and reflection spectra (similar to Fig. 2), we find that the simulations accurately reproduce the behavior of the $g^{(2)}$ measurements.

Finally, we investigate the interference between the coherently scattered single photons and the reflected laser light in more detail. By adjusting the fiber position relative to the waveguide, we can change the difference between the paths that the classical light and single-photon components travel and, thereby, controllably tune their relative phase $\phi$. Figure 4(a) shows the variation in the reflection interference spectrum as we sweep the fiber distance, realized by applying a voltage on the piezo positioner.

The photon statistics of the reflected signal depend on the relative phase $\phi$ [Fig. 4(b)]. We consider the three limit cases of constructive ($\phi = 6.28 \sim 2\pi$), dispersive ($\phi = 1.57 \sim \pi/2$), and destructive ($\phi = 3.41 \sim \pi$) interference. In the constructive interference case, single photons are added to the coherent state, resulting in sub-Poissonian photon statistics as evidenced by the measured antibunching in $g^{(2)}_{\mathrm{RR}}$ in Fig. 4(c) (top). In the dispersive and destructive interference cases, the presence of a nonzero phase makes the behavior of the photon statistics nontrivial, as the relative phase is different for the one- and multi-photon components of the coherent state. Depending on the exact phase and the relative amplitudes of the single photons and the reflected coherent state, the relative weight of the one- and two-photon components varies, resulting in either bunching or antibunching. In our regime, we observe bunching for the dispersive interference [Fig. 4(c) (middle)] and weak antibunching for destructive interference [Fig. 4(c) (bottom)]. Numerical simulations (red lines)

using our theoretical model show excellent agreement with the data.

In summary, we have presented a detailed investigation of a diamond SnV center coupled to a waveguide, showing significant transmission extinction and tunable interference between single photons and the reflected laser field as well as providing insights into the nature of the emitter-induced changes in transmitted and reflected fields through photon correlation measurements. These results highlight diamond SnV centers integrated in waveguides as a promising platform for realizing efficient integrated spin-photon interfaces.

Whereas nanophotonic cavities can provide overall much stronger interaction, the use of waveguides can alleviate significant fabrication overhead and by their broadband nature provide a more flexible platform, since they do not need to be tuned to the emitter frequency and readily allow for more centers to be used in the same device. We investigated four waveguides in this device, and all contained suitably coupled SnV centers, with measured $\Delta T$ ranging between 15% and 34%.

While our Letter shows couplings that are in line with the state of the art for color center-waveguide systems [8,18,43], further improvement can be obtained by optimizing the emitter overlap with the optical mode: The waveguide thickness and the implantation depth can be matched to get the SnV closer to the center, while localized ion implantation could improve the lateral position. Already at the established coupling, these devices, when combined with coherent spin control [15,16], may allow for remote entanglement significantly surpassing the generation rates obtained the diamond NV center [44,45], opening up new avenues for scaling quantum networks.

The datasets that support this manuscript are available at 4TU.ResearchData [46].

We thank Henri Ervasti and Pieter Botma for software support, Kevin Chen for help in processing the Sn implanted sample, Anders S. Sørensen for helpful discussions, and Yanik Herrmann and Julius Fischer for proofreading the manuscript. We gratefully acknowledge support by the Dutch Research Council (NWO) through the Spinoza prize 2019 (Project No. SPI 63-264), by the Dutch Ministry of Economic Affairs and Climate Policy (EZK) as part of the Quantum Delta NL program, by the joint research program "Modular quantum computers" by Fujitsu Limited and Delft University of Technology, cofunded by the Netherlands Enterprise Agency under Project No. PPS2007, and by the QIA-Phase 1 project through the European Union's Horizon Europe research and innovation program under Grant Agreement No. 101102140. L. D. S. acknowledges funding from the European Union's Horizon 2020 research and innovation program under the Marie Sklodowska-Curie Grant Agreement No. 840393.

[*]Present address: Sparrow Quantum, Copenhagen, Denmark.
[†]Present address: Department of Physics, Harvard University, Cambridge, Massachusetts 02138, USA.
[‡]r.hanson@tudelft.nl

[1] D. D. Awschalom, R. Hanson, J. Wrachtrup, and B. B. Zhou, Nat. Photonics **12**, 516 (2018).
[2] M. Atatüre, D. Englund, N. Vamivakas, S.-Y. Lee, and J. Wrachtrup, Nat. Rev. Mater. **3**, 38 (2018).
[3] H. J. Kimble, Nature (London) **453**, 1023 (2008).
[4] S. Wehner, D. Elkouss, and R. Hanson, Science **362**, eaam9288 (2018).
[5] M. Pompili, S. L. N. Hermans, S. Baier, H. K. C. Beukers, P. C. Humphreys, R. N. Schouten, R. F. L. Vermeulen, M. J. Tiggelman, L. Dos Santos Martins, B. Dirkse, S. Wehner, and R. Hanson, Science **372**, 259 (2021).
[6] S. L. N. Hermans, M. Pompili, H. K. C. Beukers, S. Baier, J. Borregaard, and R. Hanson, Nature (London) **605**, 663 (2022).
[7] M. K. Bhaskar, R. Riedinger, B. Machielse, D. S. Levonian, C. T. Nguyen, E. N. Knall, H. Park, D. Englund, M. Lončar, D. D. Sukachev, and M. D. Lukin, Nature (London) **580**, 60 (2020).
[8] N. H. Wan, T.-J. Lu, K. C. Chen, M. P. Walsh, M. E. Trusheim, L. De Santis, E. A. Bersin, I. B. Harris, S. L. Mouradian, I. R. Christen, E. S. Bielejec, and D. Englund, Nature (London) **583**, 226 (2020).
[9] C. Bradac, W. Gao, J. Forneris, M. E. Trusheim, and I. Aharonovich, Nat. Commun. **10**, 5625 (2019).
[10] M. Ruf, N. H. Wan, H. Choi, D. Englund, and R. Hanson, J. Appl. Phys. **130**, 070901 (2021).
[11] M. E. Trusheim *et al.*, Phys. Rev. Lett. **124**, 023602 (2020).
[12] J. Arjona Martínez, R. A. Parker, K. C. Chen, C. M. Purser, L. Li, C. P. Michaels, A. M. Stramma, R. Debroux, I. B. Harris, M. Hayhurst Appel, E. C. Nichols, M. E. Trusheim, D. A. Gangloff, D. Englund, and M. Atatüre, Phys. Rev. Lett. **129**, 173603 (2022).
[13] A. E. Rugar, S. Aghaeimeibodi, D. Riedel, C. Dory, H. Lu, P. J. McQuade, Z.-X. Shen, N. A. Melosh, and J. Vučković, Phys. Rev. X **11**, 031021 (2021).
[14] J. M. Brevoord, L. D. Santis, T. Yamamoto, M. Pasini, N. Codreanu, T. Turan, H. K. C. Beukers, C. Waas, and R. Hanson, Phys. Rev. Applied **21**, 054047 (2024).
[15] E. I. Rosenthal, C. P. Anderson, H. C. Kleidermacher, A. J. Stein, H. Lee, J. Grzesik, G. Scuri, A. E. Rugar, D. Riedel, S. Aghaeimeibodi, G. H. Ahn, K. Van Gasse, and J. Vuckovic, Phys. Rev. X **13**, 031022 (2023).
[16] X. Guo, A. M. Stramma, Z. Li, W. G. Roth, B. Huang, Y. Jin, R. A. Parker, J. A. Martínez, N. Shofer, C. P. Michaels, C. P. Purser, M. H. Appel, E. M. Alexeev, T. Liu, A. C. Ferrari, D. D. Awschalom, N. Delegan, B. Pingault, G. Galli, F. J. Heremans, M. Atatüre, and A. A. High, Phys. Rev. X **13**, 041037 (2023).
[17] H. K. C. Beukers, M. Pasini, H. Choi, D. Englund, R. Hanson, and J. Borregaard, PRX Quantum **5**, 010202 (2024).
[18] M. K. Bhaskar, D. D. Sukachev, A. Sipahigil, R. E. Evans, M. J. Burek, C. T. Nguyen, L. J. Rogers, P. Siyushev, M. H. Metsch, H. Park, F. Jelezko, M. Lončar, and M. D. Lukin, Phys. Rev. Lett. **118**, 223603 (2017).
[19] H. Thyrrestrup, G. Kiršanskė, H. Le Jeannic, T. Pregnolato, L. Zhai, L. Raahauge, L. Midolo, N. Rotenberg, A. Javadi,

R. Schott, A. D. Wieck, A. Ludwig, M. C. Löbl, I. Söllner, R. J. Warburton, and P. Lodahl, Nano Lett. **18**, 1801 (2018).
[20] S. Faez, P. Türschmann, H. R. Haakh, S. Götzinger, and V. Sandoghdar, Phys. Rev. Lett. **113**, 213601 (2014).
[21] A. Sipahigil, R. E. Evans, D. D. Sukachev, M. J. Burek, J. Borregaard, M. K. Bhaskar, C. T. Nguyen, J. L. Pacheco, H. A. Atikian, C. Meuwly, R. M. Camacho, F. Jelezko, E. Bielejec, H. Park, M. Lončar, and M. D. Lukin, Science **354**, 847 (2016).
[22] D. E. Chang, A. S. Sørensen, E. A. Demler, and M. D. Lukin, Nat. Phys. **3**, 807 (2007).
[23] J. T. Shen and S. Fan, Opt. Lett. **30**, 2001 (2005).
[24] B. Khanaliloo, M. Mitchell, A. C. Hryciw, and P. E. Barclay, Nano Lett. **15**, 5131 (2015).
[25] M. Mitchell, D. P. Lake, and P. E. Barclay, APL Photonics **4**, 016101 (2019).
[26] S. Mouradian, N. H. Wan, T. Schröder, and D. Englund, Appl. Phys. Lett. **111**, 021103 (2017).
[27] M. Ruf, Cavity-enhanced quantum network nodes in diamond, Ph.D. thesis, Delft University of Technology, 2021.
[28] See Supplemental Material at http://link.aps.org/supplemental/10.1103/PhysRevLett.133.023603, which includes Refs. [29–36], for further details on the device fabrication and the experimental setup, emitter lifetime measurements and polarization response measurements, simulations and theoretical models of the emitter-waveguide system.
[29] I. T. Raa, H. K. Ervasti, P. J. Botma, L. C. Visser, R. Budhrani, J. F. van Rantwijk, S. P. Cadot, J. Vermeltfoort, M. Pompili, A. J. Stolk, M. J. Weaver, K. L. van der Enden, D. de Leeuw Duarte, M. Teng, J. van Zwieten, and F. Grooteman, QMI—Quantum Measurement Infrastructure, a Python 3 framework for controlling laboratory equipment, 4TU.ResearchData, 10.4121/6d39c6db-2f50-4a49-ad60-5bb08f40cb52.v1.
[30] D. A. Steck, *Quantum and Atom Optics* (revision 0.16, 26 April, 2024), http://steck.us/teaching.
[31] E. Collett, *Field Guide to Polarization* (SPIE, Bellingham, WA, 2005).
[32] E. I. Rosenthal, S. Biswas, G. Scuri, H. Lee, A. J. Stein, H. C. Kleidermacher, J. Grzesik, A. E. Rugar, S. Aghaeimeibodi, D. Riedel, M. Titze, E. S. Bielejec, J. Choi, C. P. Anderson, and J. Vuckovic, arXiv:2403.13110.
[33] A. Javadi, I. Söllner, M. Arcari, S. L. Hansen, L. Midolo, S. Mahmoodian, G. Kiršanskė, T. Pregnolato, E. H. Lee, J. D. Song, S. Stobbe, and P. Lodahl, Nat. Commun. **6**, 8655 (2015).
[34] A. H. Kiilerich and K. Mølmer, Phys. Rev. Lett. **123**, 123604 (2019).
[35] J. Johansson, P. Nation, and F. Nori, Comput. Phys. Commun. **183**, 1760 (2012).
[36] F. A. M. de Oliveira, M. S. Kim, P. L. Knight, and V. Buek, Phys. Rev. A **41**, 2645 (1990).
[37] M. J. Burek, C. Meuwly, R. E. Evans, M. K. Bhaskar, A. Sipahigil, S. Meesala, B. Machielse, D. D. Sukachev, C. T. Nguyen, J. L. Pacheco, E. Bielejec, M. D. Lukin, and M. Lončar, Phys. Rev. Appl. **8**, 024026 (2017).
[38] Y. Herrmann, J. Fischer, J. M. Brevoord, C. Sauerzapf, L. G. C. Wienhoven, L. J. Feije, M. Pasini, M. Eschen, M. Ruf, M. J. Weaver, and R. Hanson, arxiv:2311.08456.
[39] T. Iwasaki, Y. Miyamoto, T. Taniguchi, P. Siyushev, M. H. Metsch, F. Jelezko, and M. Hatano, Phys. Rev. Lett. **119**, 253601 (2017).
[40] J. Görlitz, D. Herrmann, G. Thiering, P. Fuchs, M. Gandil, T. Iwasaki, T. Taniguchi, M. Kieschnick, J. Meijer, M. Hatano, A. Gali, and C. Becher, New J. Phys. **22**, 013048 (2020).
[41] M. K. Koch, M. Hoese, V. Bharadwaj, J. Lang, J. P. Hadden, R. Ramponi, F. Jelezko, S. M. Eaton, and A. Kubanek, ACS Photonics **9**, 3366 (2022).
[42] J.-T. Shen and S. Fan, Phys. Rev. Lett. **98**, 153003 (2007).
[43] R. A. Parker, J. A. Martínez, K. C. Chen, A. M. Stramma, I. B. Harris, C. P. Michaels, M. E. Trusheim, M. H. Appel, C. M. Purser, W. G. Roth, D. Englund, and M. Atatüre, arXiv:2305.18923.
[44] H. Bernien, B. Hensen, W. Pfaff, G. Koolstra, M. S. Blok, L. Robledo, T. H. Taminiau, M. Markham, D. J. Twitchen, L. Childress, and R. Hanson, Nature (London) **497**, 86 (2013).
[45] S. Hermans, Quantum networks using spins in diamond, Ph.D. thesis, Delft University of Technology, 2022.
[46] M. Pasini, N. Codreanu, T. Turan, A. Riera Moral, C. F. Primavera, L. De Santis, H. K. C. Beukers, J. M. Brevoord, C. Waas, J. Borregaard, and R. Hanson, Data underlying the publication "Nonlinear Quantum Photonics with a Tin-Vacancy Center Coupled to a One-Dimensional Diamond Waveguide," 10.4121/5ae194d5-481e-41c6-b924-679ab6-da492d.v1.